Nanoscale

Accepted Manuscript

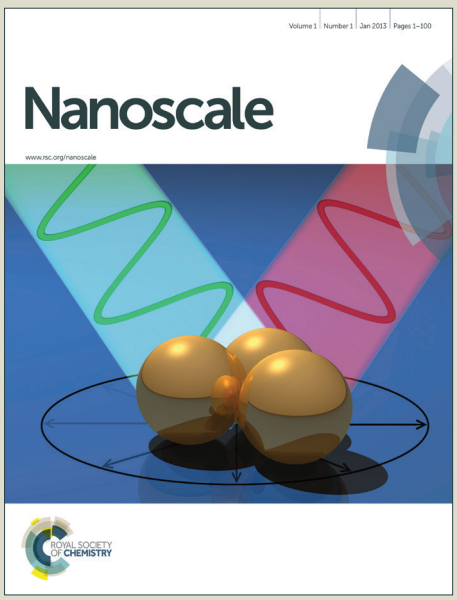

ROYAL SOCIETY OF CHEMISTRY

www.rsc.org/nanoscale

Silver Nanocube Aggregation Gradient Materials in Search for Total Internal Reflection with High Phase Sensitivity

Tobias A.F. König,[a,c] Petr A. Ledin,[a] Michael Russell,[a] Jeffrey A. Geldmeier,[a] Mahmoud. A. Mahmoud,[b] Mostafa A. El-Sayed,[b] and Vladimir V. Tsukruk[,a]*

[a] School of Materials Science and Engineering,
Georgia Institute of Technology,
Atlanta, Georgia 30332-0245 (USA)

[b] Laser Dynamics Laboratory, School of Chemistry and Biochemistry,
Georgia Institute of Technology,
Atlanta, Georgia 30332-0400 (USA)

[c] Current address:
Physical Chemistry II,
University of Bayreuth,
95440 Bayreuth (Germany)

*Corresponding e-mail: vladimir@mse.gatech.edu

Abstract

We fabricated monolayer coatings of a silver nanocube aggregation to create a step-wise optical strip by applying different surface pressures during slow Langmuir-Blodgett deposition. The varying amount of randomly distributed nanocube aggregates with different surface coverages in gradient manner due to changes in surface pressure allows for continuous control of the polarization sensitive absorption of the incoming light over a broad optical spectrum. Optical characterization under total internal reflection conditions combined with electromagnetic simulations reveal that the broadband light absorption depends on the relative orientation of the nanoparticles to the polarization of the incoming light. By using computer simulations, we found that the electric field vector of the s-polarized light interacts with the different types of silver nanocube aggregations to excite different plasmonic resonances. The s-polarization shows dramatic changes of the plasmonic resonances at different angles of incidence (shift of 64 nm per 10° angle of incidence). With a low surface nanocube coverage (from 5% to 20%), we observed a polarization-selective high absorption of 80% (with an average 75%) of the incoming light over a broad optical range in the visible region from 400 nm to 700 nm. This large-area gradient material with location-dependent optical properties can be of particular interest for broadband light absorption, phase-sensitive sensors, and imaging.

Keywords: Localized surface plasmon resonances, silver nanocubes, bottom-up assembly, total internal reflection, super absorber, phase-sensitive sensors

Table of Contents (TOC) Figure

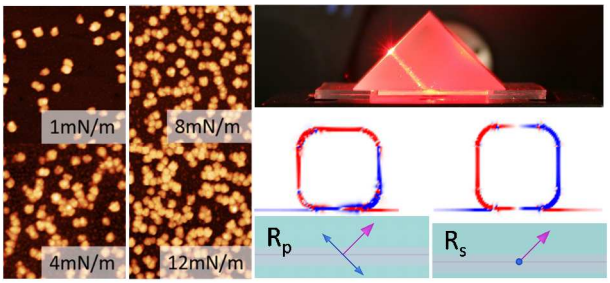

Introduction

The unique optical properties of plasmonic nanoparticles have attracted much interest in diverse scientific fields as a result of their promising applications in light harvesting,[1] biological/chemical sensing,[2, 3] metamaterials,[4] and plasmonic circuits.[5] Many concepts for plasmonic applications have been published, but they usually show a lack in scalability. For self-assembled nanoparticles, it is a non-trivial task to precisely fabricate a large number of identical particle assemblies and to precisely characterize the localized electromagnetic field enhancement.[6] Among other bottom-up approaches for the assembly of nanoparticles, the Langmuir-Blodgett (LB) technique enables the formation of molecular monolayers at the air-water interface with a controllable surface density.[7] Furthermore, this method can be used to assemble nanoparticles, which can be easily scaled up to relatively large substrates.[8]

Silver nanocubes as active components of such materials and coatings have gained much attention recently because of their complex plasmonic properties and coupling phenomena in comparison with spherical nanoparticles.[9] The flat facets of a nanocube in close contact with a dielectric substrate allow hybridized plasmonic modes to appear due to the interference of dark and bright modes.[10] Chemical and biological sensors based on this effect could result in outstanding sensitivity in aggregated systems.[11,12] Further potential advantages such as fluorescence enhancement,[13, 14] waveguide modes,[15] electrically tunable plasmonics,[16] and ideal absorbance[17] have been observed in complex materials systems with strong coupling between the nanocubes and a supporting metallic film or grating separated by an ultrathin spacer layer.[18, 19] To form an ideal light absorber in a broad range, the reflection and transmission must be controlled, which could result in improved efficiency, for instance, in thin film solar cells.[1] A general concept of topological darkness has been established which is based on local plasmonic field enhancements and the phase change of the interacting light.[20] In other words, a zero reflectance (ideal absorber) material yields sharp phase changes,[21] which allow the film-coupled nanocubes (on a dielectric or on a metallic film) to be used in two important fields: super absorption and phase-sensitive sensing.

Theoretical studies predict the super absorption of a single layer of well-spaced, periodically arranged noble metal nanoparticles.[22] Experimental studies from the Fery group show a substrate-supported technique, which enables the fabrication of periodic, well-spaced, and large-area nanoparticle systems at low costs.[23] Recently, the Käll group has realized complete light annihilation for a narrow bandwidth and for a specific polarization with gold nanodisks fabricated by hole-mask colloidal lithography.[24] In order to achieve a broadband and polarization independent super absorption[25] it is necessary to use self-oriented nanocubes[26] with a bottom-up fabrication technique. Consequently, the challenge is to build an active coating with well-spaced nanoparticles and with control over the aggregation type, which enables light trapping on the length scale below the diffraction limit for large areas.

Few investigations have been done for low surface coverage of metallic nanoparticles randomly distributed on a transparent substrate (<25%). This ultra-thin coverage with metallic nanoparticles shows manifold critical-coupling conditions compared to a solid metallic film. So far, the critical optical properties of aggregations and their relative orientation in respect to the plane of incidence have not been investigated. Therefore, we used a bottom-up, lithography and template-free, and easily scalable LB deposition to design silver nanocube aggregation gradients on a large centimeter scale area of solid substrates. The nanocubes were deposited on a quartz slide in the form of optical strip with controllable (step-wise) surface coverage to obtain multiple plasmonic resonances which originate from the different nanocube aggregations types. Relatively uniformly spaced silver nanocubes with different types of aggregation allows to obtain active hybrid coatings with absorption of virtually all incoming light, which occurs with a high phase shift.

Experimental

Silver nanocube synthesis: Silver nanocubes (AgNCs) with a 54 nm edge length were synthesized using the polyol method as described elsewhere.[27] Briefly, in a 100 mL round bottom glass flask, 70 mL of ethylene glycol (EG) was heated to 150 °C

for 1 h. Then a solution of 0.85 g poly(vinylpyrrolidone) (PVP) was dissolved in 10 mL EG and added to the hot EG. 0.4 mL of sodium sulfide (Na_2S) (3 mM) dissolved in EG and 6 mL of 282 mM silver nitrate dissolved in EG were injected into the reaction mixture. The reaction mixture was stirred at 200 rpm and refluxed at 150 °C for 10 minutes until the solution became opaque. In order to purify the AgNCs, 5 mL of the prepared AgNC solution was diluted with water and centrifuged at 10,000 rpm for 5 minutes. The precipitated AgNCs were then re-dispersed in water. The synthesized AgNCs were 54.0±6 nm as statistically evaluated using TEM images as discussed earlier.[16] The AgNCs were also covered by a PVP layer (refractive index taken from reference [16]) as described in the synthetic procedure, and the coating thickness was statistically determined to be 1.5±0.3 nm.[28]

Step-wise assembly of AgNCs on quartz substrate *via* LB method: A KSV2000 LB minitrough filled with Nanopure water (18.2 MΩ cm) at room temperature was used for LB deposition. The surface pressure was measured with a platinum Wilhelmy plate attached to a pressure sensor. The quartz slides (CGQ-0640-01, 75×25 mm) were purchased from Chemglass Life Sciences. The quartz slide (cleaned with acetone and by O_2 plasma etching for 1 min at 100 μTorr (0.13 mbar)) was submerged into a water phase prior to the formation of a monolayer. The stock solution of PVP coated AgNC in water (1 mL) was diluted to 10 mL using deionized water (18.2 MΩ cm) in a conical-bottom glass centrifuge tube. The AgNCs were separated by centrifugation for 30 min at 4,000 rpm and subsequently washed in a similar manner with EtOH/H_2O (10 ml, 1/1, v/v) and EtOH (10 mL).

Finally, the residue was suspended in $CHCl_3$ (2 mL) and used within 1 h for LB deposition. The solution of AgNCs in $CHCl_3$ (1 mL) was carefully spread over the water surface and the monolayer was left for 30 min to allow for evaporation of the organic solvent and equilibration. The nanoparticles in chloroform solution spread as a monolayer on an air-water interface and formed aggregates with different surface coverages as controlled by the surface pressure.[29, 30] The Langmuir monolayer of AgNCs was then compressed at a rate of 5 mm/min to reach a surface pressure of 1 mN/m.The monolayer was transferred onto quartz slide at the air-water interface by

pulling the substrate up vertically at a rate of 1 mm/min. After a vertical distance of 15 mm of deposition, the AgNC monolayer was compressed further at a rate of 5 mm/min to reach the surface pressure of 4 mN/m and was transferred onto next 15 mm of the quartz slide by pulling the substrate up vertically at a rate of 1 mm/min. The same procedure was repeated at the surface pressures 8 and 12 mN/m in order to create step-wise gradient in vertical direction (Figure 1). Since both sides of the quartz slide were coated with a monolayer, one side and the edges were carefully cleaned with acetone to remove the silver nanocubes on that side. All samples were stored in a vacuum desiccator before characterization.

The prepared slide with the AgNC monolayer gradient was characterized with UV-Vis spectroscopy (Shimadzu UV-2450 spectrophotometer over a wavelength range of 300-1000 nm) and atomic force microscopy (AFM). AFM scanning of the silver nanocubes was conducted using a Digital Instrument Dimension 3000 in tapping mode at a resolution of 512x512 pixels. Scans were performed at a rate of 0.5–1.0 Hz for surface areas of 5×5 μm and 10×10 μm according to the usual procedure adapted in our lab.[31] Silicon nitride AFM tips (MikroMasch) with a spring constant of 7 N/m and a resonant frequency of ca. 150 kHz were used for AFM imaging. We used the AFM images for statistical analyses of nanocube aggregates (about 800 aggregates) and inter-particular distances and surface coverage.

Spectral ellipsometry and total internal reflection measurement: Ellipsometric parameters and reflection measurements for the AgNC films were obtained with a M2000 spectroscopic ellipsometer from Woollam Co. in a reflection over a wavelength range of 300-1000 nm using both s- and p-polarized light at incident angles of 45, 50, and 60^{o}. We employed a CaF_2 prism (25 mm base, right angle, uncoated) purchased from Thorlabs for total internal reflection measurements. A single drop of diethylene glycol was applied to the bottom of the prism as immersion oil where the opposite (uncoated) side of the AgNC covered quartz slide made contact. Care was taken with proper coverage of immersion oil to ensure no air gaps occurred at the prism-slide interface. The prism-oil-slide setup was mounted on the ellipsometer stage with the

AgNC coating facing down, making no contact with the stage (see Supporting information). As a control, an uncoated quartz slide was measured for every incident angle and polarization measurement.

Statistical analysis of AgNC aggregates: The surface coverage and aggregate fraction of samples were calculated from AFM images using *ImageJ* particle size analysis. A color threshold filter was used to produce a binary image that considered any cluster of nanocubes touching as a single particle with a corresponding measured area. Only the pixels highlighted by the color threshold filter were included in area measurements to account for any holes from large nanocube aggregations. From the binary image, both nanoparticles entirely within the image frame and those on the edge were considered for surface coverage calculations. To correct for artificially larger particle sizes introduced by the AFM tip convolution and image processing (e.g. color threshold filter), the average area for a single nanocube for a given image was calculated and divided by the average area for a single nanocube of 3,025 nm^2 (as measured by transmission electron microscopy (TEM)). Thus, adjusted values for surface coverage and number of AgNCs per square micron were computed. In order to calculate the fraction of particle aggregation type, the same binary images of particles previously mentioned were utilized. However, nanoparticles along the edges that were only partially visible in the AFM image frame were excluded from particle size analysis since the aggregation type could not be known. The resulting data were binned into X-mers by area in nm^2. Any counted nanoparticle under 3,000 nm^2 was disregarded as an image artifact. Any particles in the range of 3,000-9,000 nm^2, 9,000-15,000 nm^2, 15,000-21,000 nm^2, 21,000-30,000 nm^2, 30,000-39,000 nm^2, 39,000-48,000 nm^2, and larger than 48,000 nm^2, were defined as a monomer, dimer, trimer, tetramer, pentamer, hexamer, and n-mer, respectively.

The fraction of each type of aggregate for different LB surface pressures was then calculated and used to construct histogram of aggregation distribution. There are multiple counts for each aggregate and these are found through their area measurements, so statistical error in the analysis of AgNC aggregates can be sourced from these measurements. In this case, the mean area of each particle aggregation

type has a standard deviation associated with it. Finding the standard error is simply dividing the standard deviation by the square root of the number of counts for each aggregate type. Then, a relative standard error is found through dividing the standard error by the mean value. These values (percentages) are then multiplied by the fraction aggregate type to provide values for error bars.

Hyperspectral measurements: In order to directly compare simulation results for AgNC aggregates to experimental ones, AgNCs were spin-cast in a dilute solution to more easily identify specific aggregates and single cubes. The solution from previous steps was diluted by a factor of 10 in chloroform and spin-cast on a quartz substrate at 2,000 rpm. We used these samples for analysis of individual spectral signatures because the concentration of AgNCs from LB deposition is too high to clearly separate individual nanoparticles and aggregates. AFM was used to spatially characterize the AgNCs and identify individual nanoparticles and types of aggregates while hyperspectral microscopy enabled the collection of spectra from single nanoparticles and aggregates.

Hyperspectral images were collected using a CytoViva Hyperspectral imaging system with a diffraction grating spectrophotometer wavelength range of 400-1,000 nm (spectral resolution of 2.8 nm). A tungsten halogen lamp with an aluminum reflector and a wavelength range of 450-850 nm was used in conjunction with a CytoViva dark field transmission collimator as a light source. A 100x dark field objective (NA: 0.90) was used to collect transmission measurements by scanning the surface with a 10 nm step size scan resolution and a 1 s integration time. Hyperspectral maps of the samples were normalized to the lamp spectrum collected with a blank quartz slide. About 20 pixel spectra were collected from individual aggregates and averaged to obtain aggregate spectra. Roughly, 25,000 pixel spectra were collected for an averaged monomer spectrum. All experimental spectra were smoothed with an adjacent averaging window of 15 points (17 nm wavelength span) in order to eliminate instrumentation effects.

FDTD simulations: Simulations of the extinction (extinction = scattering + absorption) spectra and the reflection were done using commercial software from Lumerical

Solutions Inc. (FDTD Solutions, Version 8.0.2). The edge-rounding factor used in this simulation is defined as the edge radius scaled by the length of the nanocube edge. For the modeling, the edge-rounding factor was estimated to be 25 %. Each washing step induced a blue shift of the dipole resonance which is based on an increase of the edge-rounding factor.[16] The nanocube coating thickness was chosen as 1 nm or 2 nm in FDTD simulations due to the integer mesh size limitations. Consequently, the minimum cube-to-cube distances were selected as 2 nm and 4 nm, respectively. The polymer coating was rounded at the cube edges to the same degree as the silver nanocubes for simulations. The refractive index of the quartz glass substrate purchased from Chemglass was measured with a spectroscopic ellipsometer (Supporting Information, Figure S1a). We included the glass substrate below the nanocubes and the stabilizing layer (PVP coating) as shown in the Supporting Information (Figure S1b).

For silver permittivity, we used material data from Hagemann *et al.* (CRC approximation).[32] We found a much better agreement with our experimentally measured extinction spectra by using the permittivity from the CRC approximation instead of the more commonly used source from Johnson and Christy (JC).[33] The significant difference between JC and CRC is the lower imaginary component of the permittivity for the JC data. A lower imaginary component results in a narrower LSPR peak and a higher extinction cross-section but does not change the plasmonic peak location. The higher imaginary component in the permittivity from the CRC approximation can be attributed to geometrical effects as Shalaev *et al.* have reported.[34] For broadband source simulations, the FDTD software approximates the refractive index of the materials by a built-in function. The fitting parameters for all materials gave an RMS error <0.2. A simulation mesh size of 1 nm was chosen and the second conformal variant mesh refinement was used. For the best simulation stability, the mesh area was chosen to be 120 nm larger than the existing structure in all three principal directions. All simulations reached the auto shut off level of 10^{-4} before reaching 75 fs simulation time. Boundary conditions and the angle of incidence were chosen differently for extinction spectra modeling (perfectly matched layer (PML) for all

boundaries at normal incidence) and simulation in reflection with Bloch boundary condition for lateral directions used only at total internal reflection angles.

Results and Discussion

Silver nanocube aggregation gradients

We fabricated silver nanocube aggregation gradients in the form of optical strips with step-wise changes in surface coverage with the help of a conventional LB technique as described above (Figure 1). After spreading the nanocubes on the water-air-interface and applying minimum pressure, the nanocubes were mostly separated as monomers (individual nanocubes). As seen from optical images and AFM images, the surface coverage increased in a step-wise fashion with an increase in the applied surface pressure from top to bottom (Figure 1b). Increasing the pressure, the cubes begin to aggregate, preferentially face-to-face, as has been shown in solution by Klinkova et al.[35] We found no evidence for a preferred orientation of the aggregations on the LB trough or on the quartz slide, which would result in grating effects or polarization dependence at normal incidence (see Supporting Information, Figure S2). Consequently, we consider the silver nanocube aggregations as randomly distributed on the quartz slide.

We quantified the apparent increase of nanocube aggregations and the increase in surface coverage up to 20% with an increasing surface pressure in Figure 2a. The fraction of aggregation type as evaluated from image analysis shows a decrease of monomer content and a corresponding increase of dimers, trimers, tetramers, pentamers, and hexamers, and n-mers when the surface pressure is increased up to 12 mN/m with multiple aggregate types dominating at higher surface pressures (Figure 2b). Statistical errors are included in Figure 2 with more details provided in the experimental part.

The role of materials parameters in total light annihilation

The total internal reflection (TIR) regime occurs at an angle of incidence beyond the critical angle of incidence of a quartz glass-air-interface (>43°). The definition of p-polarized light (electric field vector in the plane of incidence) and s-polarized light (electric field vector perpendicular to the plane of incidence) is included in Figure 1a. More details about the optical setup can be found the experimental section and Figure S3 in the Supporting Information. The elliptical spot size of the instrument is 5 mm in diameter to ensure the scalability and the large-scale usability of the silver nanocube aggregation gradient. Optical light annihilation, which includes minimum reflection and transmission, occurs at a specific frequency, polarization, and angle of incidence, and a significant challenge is to make it independent of these parameters.[1, 24] Before we go into details of the normalized reflection coefficients R_p and R_s, the measurement of the ellipsometric paramters Ψ (amplitude component) and Δ (phase difference) summarize the optical response of the fabricated coatings (Figure 3).

The ellipsometric parameters are defined through the complex reflectance ratio $r_p/r_s = \tan\Psi\, e^{i\Delta}$ where $r_p = E_p/E_i$ and $r_s = E_s/E_i$ are the amplitude reflection coefficients for parallel (p) and perpendicular (s) polarized light relative to the plane of incidence. Index i indicates the electric field of the incident light. The normalized reflection R is defined as reflected intensity scaled by incident intensity. From the complex reflectance ratio, it follows that Ψ goes to zero any time r_p goes to zero and Ψ goes to 90° any time r_s goes to zero. Based on these definitions, we observe in Figure 3a that the reflected p-polarized light goes to a minimum at ~400 nm and the reflected s-polarized light goes to zero at ~420 nm and 600 nm. These wavelengths are related to specific plasmonic modes of the higher dipolar plasmonic mode (300 nm),[28] the anti-bonding mode (~400 nm), the bonding mode (~420 nm)[10, 12] and the aggregation mode (600 nm).[16] Each localized surface plasmon resonance occurs with a change in the phase, which can be seen from the significant slope change of the phase difference as presented in Figure 3b. A significant phase shift is of particular interest for a phase-sensitive plasmonic detection and is the highest here for a deposition surface pressure of 8 mN/m.[36] The ellipsometry spectra can be deconvoluted into specific plasmonic modes to discuss the nature of their origin.

Optical response at normal incidence of the silver nanocube aggregation gradient

To understand the optical response of silver nanocube aggregates and their role in light annihilation, a detailed discussion of their measured and modelled extinction spectra is necessary (Figure 4). All extinction spectra of the silver nanocubes on a quartz glass substrate show a typical signature of the optical interband transition at 312 nm.[37] A silver nanocube with a 54 nm edge length, rounded edges/corners, and suspended in a homogenous medium shows four dominant dipolar plasmonic modes (Figure 4b). Between the energetically lowest mode (dipolar mode) and energetically highest mode, which is located above the interband gap of silver (300 nm), the missing two modes appear as a left shoulder of the dipolar mode.[28] If the nanocube is in close contact with a dielectric substrate, the dipolar mode is hybridized into a bonding mode (405-410 nm) and an anti-bonding mode (380 nm).[10, 12]

The coupling of two silver nanocubes in close contact (2 nm) might result in a so-called peak splitting.[38, 39] Such splitting was not clearly observed in conventional absorption spectra but can be detected with spectra from individual aggregation types (Figure 4a). The additional broad peak within 580-645 nm appears for aggregated nanocubes (Figure 4b). The position and the width depend upon aggregation conditions and it can be represented as a weighted superposition of plasmonic modes resulting from self-assembled cubes with different chain lengths.[12] Theoretical simulations of specific plasmonic contributions from nanocubes aggregations at an inter-particle spacing of 2 nm with different chain lengths allows the deconvolution of the experimental aggregation peak into contributions from dimers, trimers, tetramers, pentamers, and decamers and thus analysis of the extinction properties of different individual chain-like aggregates (Figure 4b). For particle aggregates from chains longer than two particles, the energetically lowest mode is called a super-radiant mode, whereas all energetically higher modes are called sub-radiant modes (Figure 4b).[40, 41] The shift of the super-radiant mode converges with an increasing particle chain length to a specific wavelength in the far infrared, which is typically reached for aggregates from 10 particles.[42, 43]

Experimental evidence for the peak splitting and shifting can be found in hyperspectral imaging (dark field) in combination with AFM imaging of the same surface area, which allows for precise identification of specific aggregates and their spectral signatures (Figure 5a). To compare the dark field measurements (Rayleigh scattering) with the simulated results of different types of silver nanocube aggregations, we included all scattering cross-sections in the supporting information (Figure S4). For example, for a selected dimer aggregate which is identified by spectral mapping and an AFM image from the same area, the local spectrum clearly shows the splitting phenomenon which is predicted by the simulated scattering cross-section (Figure 5b). Other combinations of nanoparticles into different types of aggregates result in significant shifts in plasmonic peak positions that contribute to the appearance of a broadband cross-section for nanocube coatings. Overall, as seen from the experimental spectra, AFM images, and statistical analysis, nanocube coatings with specific inter-particle spacings, the number of nanocubes present in individual aggregates, and aggregates with different chain lengths can all be adjusted by varying the surface pressure and transitioning from a gas- to liquid and then to ordered state within the LB monolayer.

Separation in p-polarized and s-polarized reflected light

An exposure of the silver nanocube gradient coatings to polarized light under TIR conditions allows the study of different optical responses which are dependent on the electric field polarization vector (Figure 6). For instance, in a thin metallic film surface plasmon polaritions can be excited under specific mode matching conditions, such as using the proper wavelength or angle of incidence.[44] The electric field component in the plane of incidence (p-polarized) has to match with the collective electron oscillation in the metal to excite the plasmonic resonance. At the same time, the s-polarized component remains unaffected. In the setup discussed here, the silver nanocube aggregations are sensitive to both polarization states. Reflection measurements in p-polarized TIR (Figure 6a) show a clear signature of higher plasmonic mode (300 nm), hybridized modes (~400 nm) and a slight response from nanocube aggregations (550 nm). On the other hand, the s-polarized TIR shows a similar response with a very pronounced absorption for the aggregation mode ~650 nm (Figure 6b). This absorption

behavior correlates with the surface coverage controlled by the surface pressure and reached its optimal absorption at a surface pressure of 8 mN/m (about 20% surface coverage). The dependence of the TIR optical response on the surface pressure and consequently the fraction of cube aggregates suggests that the orientation of the aggregates relative to the plane of incidence is of particular importance.

We have to point out that the nanocube aggregates on the substrate are randomly distributed at different surface pressures. However, electromagnetic simulations allow the distinction between two local orientation states, which are shown in Figure 7. We define the two orientation states as horizontal and vertical in respect to the plane of incidence. The optical response is fully described with these two orientation states. Both reflection spectra for a monomer reveal the same plasmonic response where for s-polarized light the minimum is achieved more readily (Figure 7a). The reflectance minimum value for p- and s-polarized light (both at 410 nm wavelength) is 0.07 and 0.02, respectively. As expected, simulations of dimers and trimers with s-polarized light confirm the experimentally measured broadband absorption of the aggregation peak. Furthermore, both the dimer aggregation and square aggregated tetramers contribute to the spectra. In previous work, we deconvoluted the extinction spectra of silver nanocube aggregates, which are located on a glass substrate in detail.[12] It is worth to note that a square aggregated tetramer shows the same longitudinal signature as a dimer but differences could be found in the cross-section intensity, which are doubled for a square aggregated tetramer compared to a dimer. The simulated reflection dip of the aggregation peak is not as smooth as observed experimentally, which can be explained by the selective simulation of two aggregates and a fixed inter-particle spacing. Our simulations suggest that the s-polarized component is sensitive to the type of aggregations (mode matching). However, under real experimental conditions, a combination of factors, such as the aggregation type varying from dimers to pentamers (and even higher), different observed inter-particle spacings, and averaging over large surface areas smooth out the individual plasmonic responses but still show major differences in polarization-dependent absorption of different nanocube coatings (Figure 7).

The mode matching with s-polarized light and the vertical orientation of the aggregates can be explained by the nature of the electric field vector of s-polarized light (E_s). The absolute value of the s-polarized vector is always constant, whereas the parallel component of the p-polarized vector changes with the angle of incidence. For instance, in surface plasmon polaritons, the parallel component at the interface (p-polarized) is responsible for the excitation of the plasmonic resonance. Consequently, the plasmonic resonance can be tuned by the angle of incidence at a fixed wavelength.[45] Here, we have a match of the s-polarized component with the silver nanocube aggregation, whereas the electric field component is parallel to the geometric axis of the aggregate. In other words, the plasmonic resonance of the s-polarized light in total internal reflection is tuned by the type of aggregations. As shown in Figure 3, we observe plasmonic resonances that are excited either by p-polarized or s-polarized light which are triggered by the silver nanocube aggregations. These results could lead to new phase-sensitive detectors, which are sensitive for both polarization states (enable a higher lateral resolution) as discussed in the following section.

Silver nanocube aggregation gradient for tunable broadband light absorption

Figure 8a shows the reflectance of an assembled silver nanocube aggregation gradient for broadband light absorption at different angles of incidence. We chose the best broadband absorption sample transferred to the quartz substrate at 8 mN/m surface pressure, which corresponded to a 20% surface coverage. The signatures of the various plasmonic resonance modes are clearly visible, whereas the plasmonic modes around 400 nm slightly increase in reflectivity and the aggregation peak red-shifts with an increasing angle of incidence (45, 50 and 60°). The same trend was also observed in the electromagnetic simulations for a dimer in horizontal and vertical orientations (Figure 8b). Furthermore, with simulations we can clearly distinguish between the absorption originated from the horizontal and vertical orientation of a nanocube dimer. Consequently, we found that the absorption of the aggregate mode at s-polarization can be tuned by 64 nm of wavelength per 10° angle of incidence. These properties could be selectively used with anisotropically oriented nanoparticles, which could be fabricated with template-assisted self-assembly methods.[8] The absorption at a high angle of

incidence is interesting for solar cell applications, particularly for capturing the sunlight in the evening and during cloudy days.[46]

Conclusions

In conclusion, we fabricated gradient-like monolayer coatings of silver nanocubes with varying amounts of aggregates (surface coverage from 5 to 20%) and studied their variable light reflection properties. The plasmonic modes of monomers and aggregates were analyzed experimentally using hyperspectral imaging and were confirmed with FDTD simulations to be an assortment of hybridized, higher dipolar, and aggregate modes. TIR measurements as well as FDTD simulations established that an increase in aggregates along with a gradually changing surface coverage of silver nanocubes allows for the control of the absorption of the incoming light over a broad optical spectrum. Moreover, silver nanocube aggregates were found to be polarization sensitive and excited different plasmonic resonances based on their relative orientation to either incident s- or p-polarized light. In particular, the s-polarization showed a high sensitivity of the aggregate plasmonic resonance to the angle of incident light (64 nm shift per 10° increase of the angle of incidence) and also contributed to a broadband high absorption of 80% of the incoming light over a broad optical range from 400 nm to 700 nm. These large-area variable optical coatings may be of particular interest for broadband light absorption and phase-sensitive sensing for large-area (centimeter scale) coatings with position-dependent light absorption.

Acknowledgements

Financial support from the U.S. Department of Energy, Office of Basic Energy Sciences, Division of Materials Sciences and Engineering under Award # DE-FG02-09ER46604 is gratefully acknowledged. We thank the Partnership for an Advanced Computing Environment (PACE) for computer resources. We thank Kevin Fan for statistical analyses of the silver nanocube aggregation.

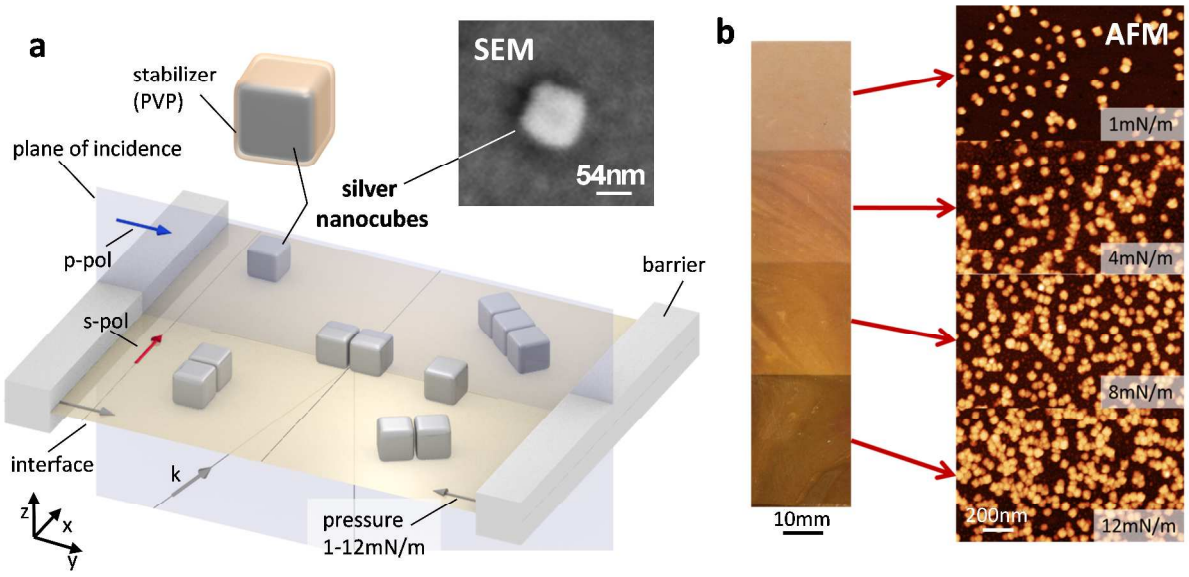

Figure 1: Silver nanocube aggregation gradient fabricated with step-wise LB deposition on a macroscopic quartz glass slide. Experimental setup (a) and optical image of the aggregation gradient (b: left) and corresponding representative AFM images from different regions (b: right). Optical characterization in total internal reflection was conducted from the backside. Arrows are defined in respect to the plane of incidence: wave vector (k), electric field vector for p-polarized (blue) and s-polarized light (red).

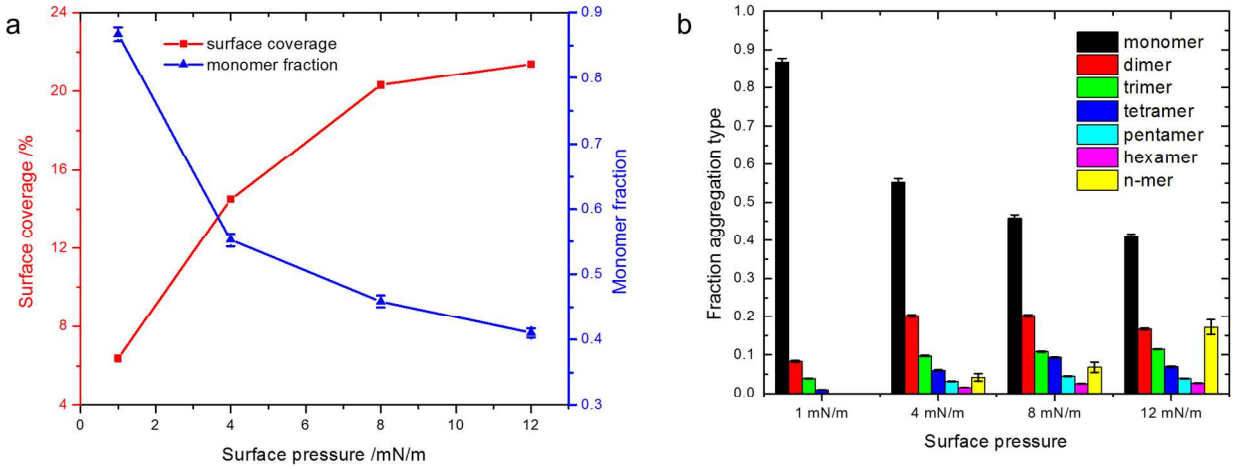

Figure 2: (a) Surface coverage and the fraction of monomers *vs.* LB surface pressure. (b) The fraction of each aggregate type in different regions with variable surface pressure.

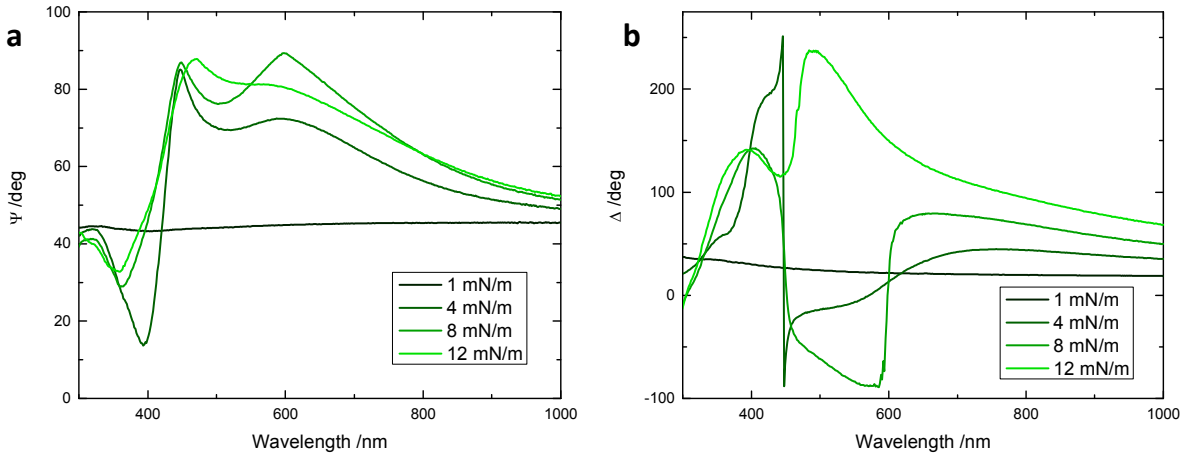

Figure 3: Spectral ellipsometric measurements in total internal reflection for ψ (a) and Δ (b) observed at surface pressures between 1 mN/m and 12 mN/m.

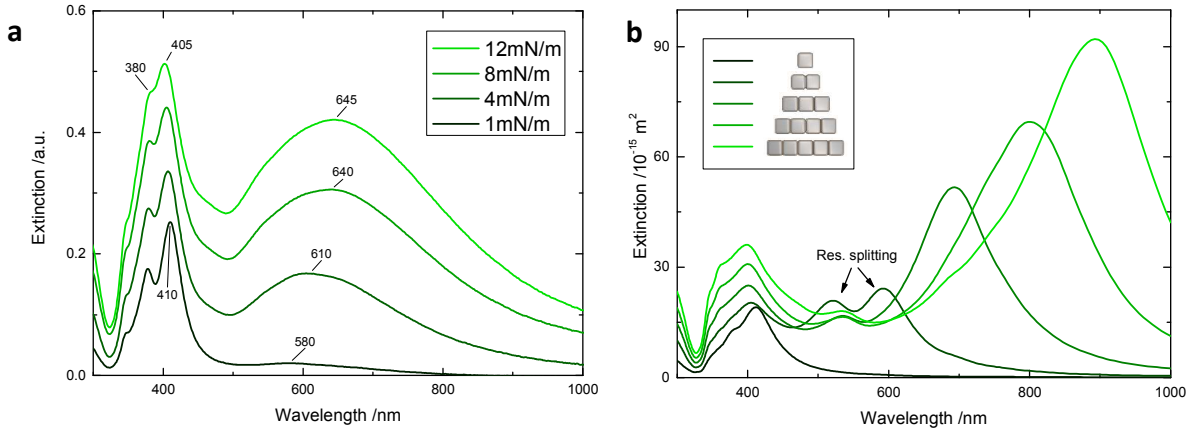

Figure 4: Experimental extinction cross-sections for LB monolayers deposited under different surface pressures (a) and simulations of different aggregation types at an inter-particle spacing of 2 nm (b).

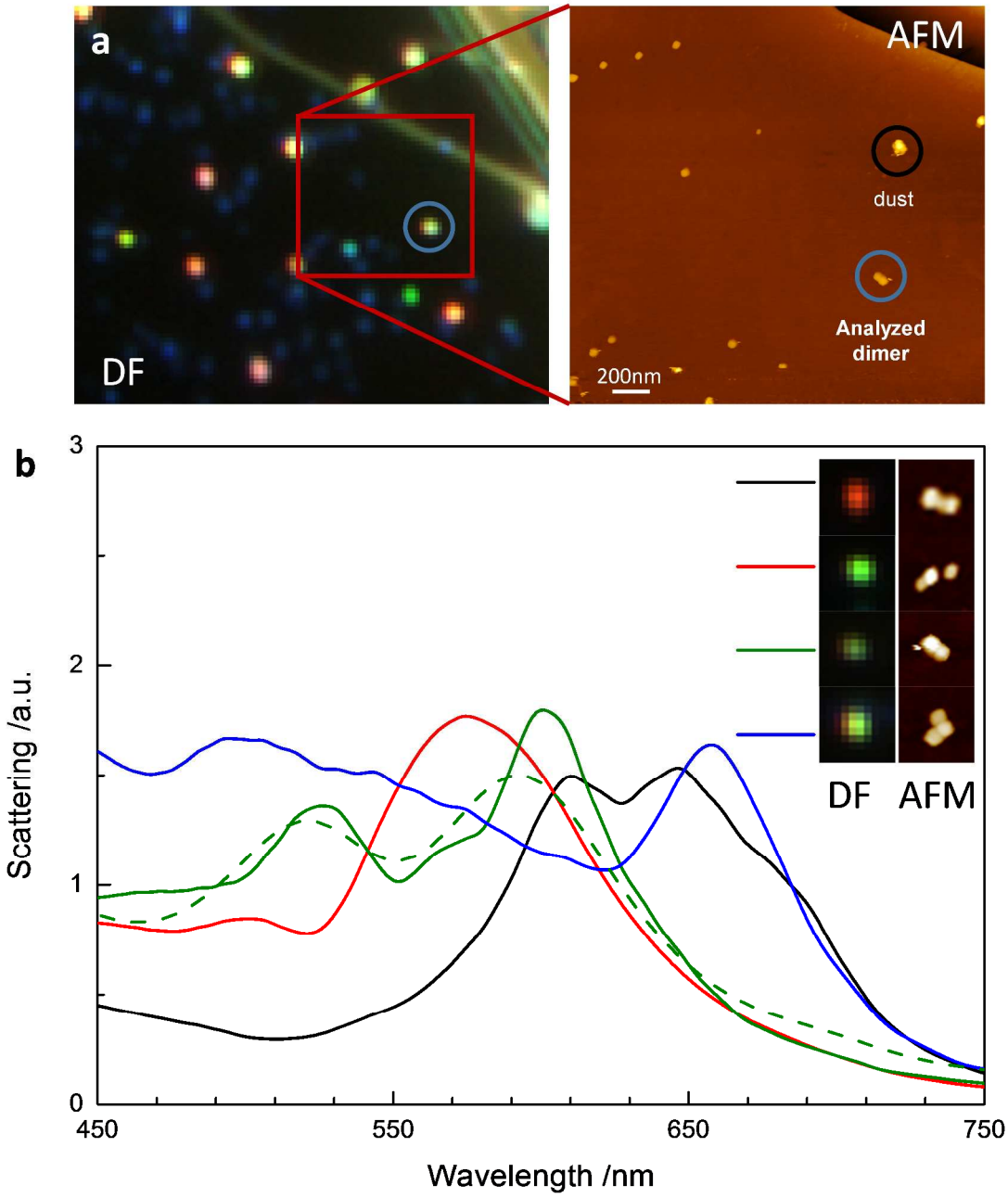

Figure 5: (a) Optical image of area selected for hyperspectral measurements (dark field, DF) of silver nanocube dimer with AFM image overlay detailing exact composition of particle aggregates analyzed and (b) hyperspectral data for a selection of different types of aggregations that demonstrates resonant peak splitting as predicted by simulation for nanocube dimer (dashed line).

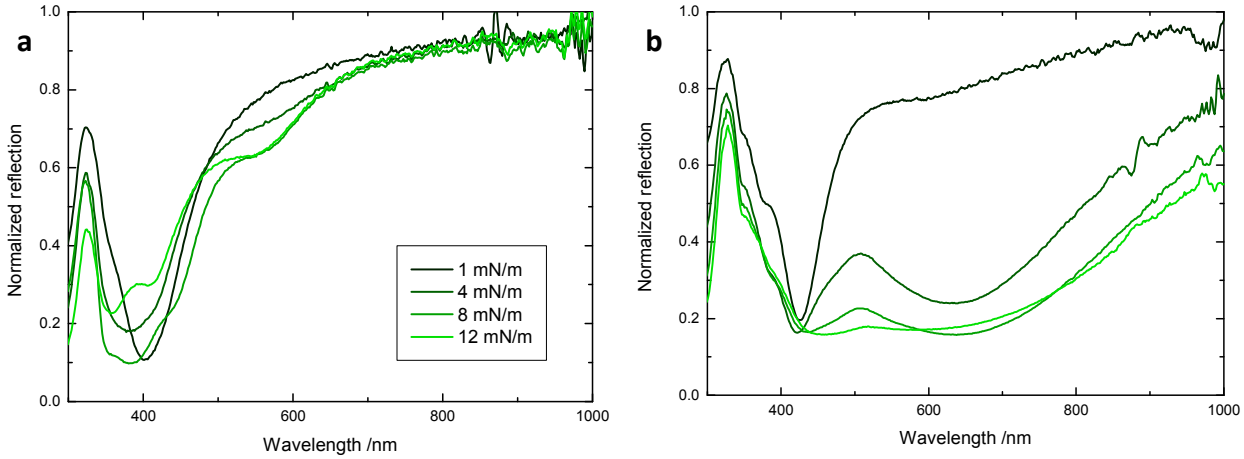

Figure 6: Normalized reflection of the nanocube aggregation gradient observed for p-polarized (a) and s-polarized (b) light at a fixed 45° angle of incidence.

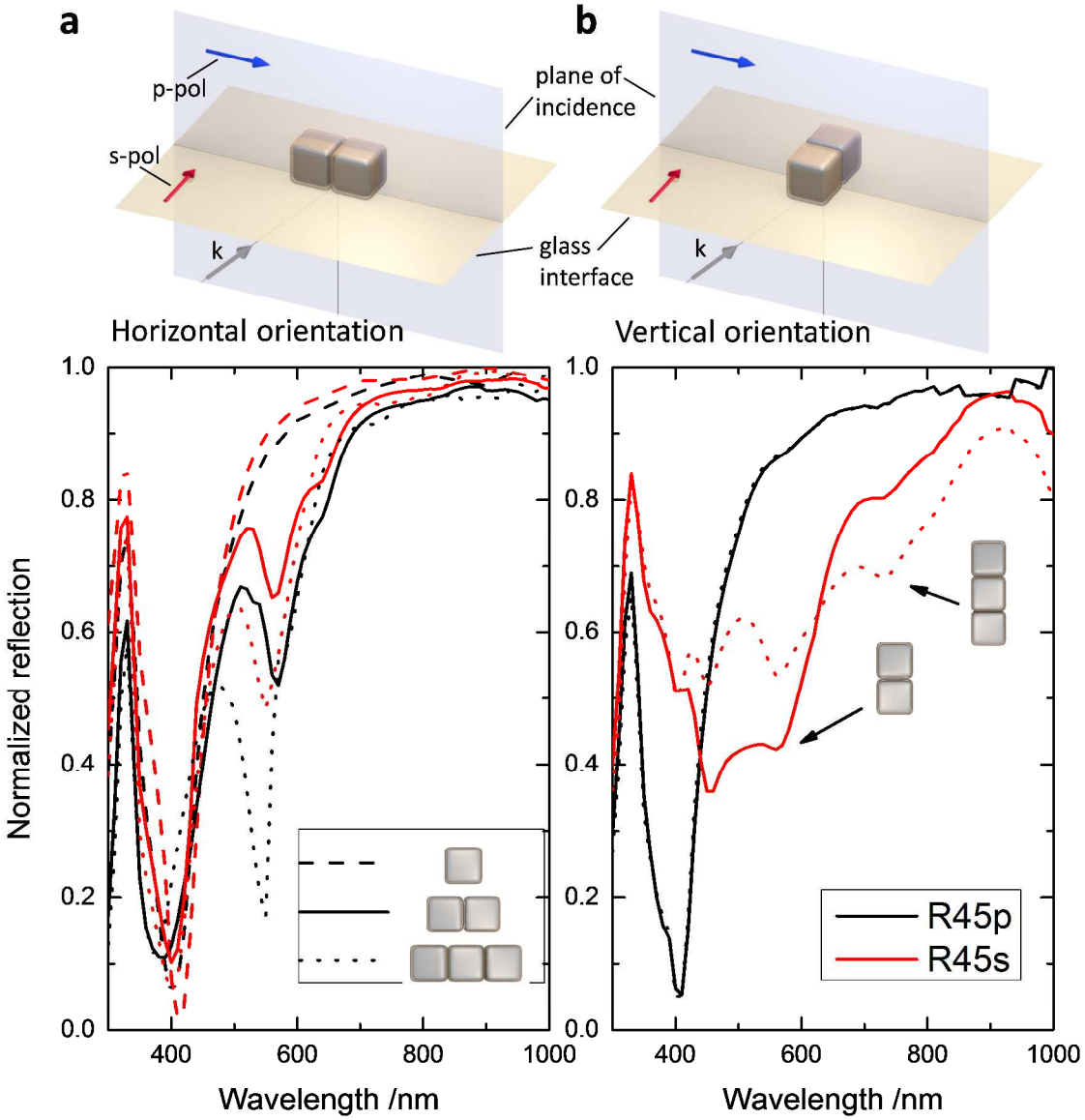

Figure 7: Optical setup of two aggregation orientations and simulated reflection for monomer, dimer, and trimer assembly. (a) Geometric axis of the cube assembly parallel to the plane of incidence (horizontal orientation) and (b) perpendicular to the plane of incidence (vertical orientation). The angle of incidence is constant at 45°. The arrows indicates the wave vector (k), electric field vector for p-polarized (blue) and s-polarized light (red).

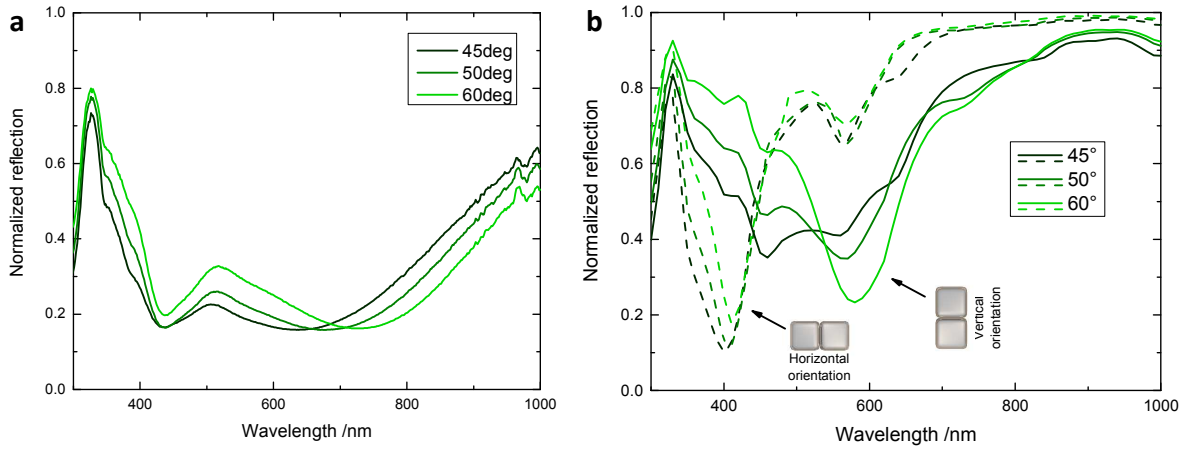

Figure 8: Experiment and simulation of a broadband total light annihilation shown at different angles of incidence and fixed s-polarization. (a) Experimental measured reflection for the optimal sample with 20% surface coverage (8 mN/m). (b) Simulations are constrained to dimers in horizontal and vertical orientations only.

References

1. H. A. Atwater and A. Polman, *Nat. Mater.*, 2010, **9**, 205-213.
2. J. Homola, S. S. Yee and G. Gauglitz, *Sens. Actuator B-Chem.*, 1999, **54**, 3-15.
3. K.-S. Lee and M. A. El-Sayed, *J. Phys. Chem. B*, 2006, **110**, 19220-19225.
4. S. Zhang, D. A. Genov, Y. Wang, M. Liu and X. Zhang, *Phys. Rev. Lett.*, 2008, **101**, 047401.
5. L. Martin-Moreno, *Nat. Phys.*, 2009, **5**, 457-458.
6. J. M. Romo-Herrera, R. A. Alvarez-Puebla and L. M. Liz-Marzan, *Nanoscale*, 2011, **3**, 1304-1315.
7. K. Ariga, Y. Yamauchi, T. Mori and J. P. Hill, *Adv. Mater.*, 2013, **25**, 6477-6512.
8. T. Kraus, D. Brodoceanu, N. Pazos-Perez and A. Fery, *Adv. Func. Mater.*, 2013, **23**, 4529-4541.
9. L. J. Sherry, S.-H. Chang, G. C. Schatz, R. P. Van Duyne, B. J. Wiley and Y. Xia, *Nano Lett.*, 2005, **5**, 2034-2038.
10. S. Zhang, K. Bao, N. J. Halas, H. Xu and P. Nordlander, *Nano Lett.*, 2011, **11**, 1657-1663.
11. N. Ahamad, A. Bottomley and A. Ianoul, *J. Phys. Chem. C*, 2011, **116**, 185-192.
12. T. König, R. Kodiyath, Z. A. Combs, M. A. Mahmoud, M. A. El-Sayed and V. V. Tsukruk, *Part. Part. Syst. Char.*, 2014, **31**, 274-283.
13. A. Rose, T. B. Hoang, F. McGuire, J. J. Mock, C. Ciracì, D. R. Smith and M. H. Mikkelsen, *Nano Lett.*, 2014, **14**, 4797-4802.
14. M. Lisunova, M. Mahmoud, N. Holland, Z. A. Combs, M. A. El-Sayed and V. V. Tsukruk, *Journal of Materials Chemistry*, 2012, **22**, 16745-16753.
15. J. B. Lassiter, F. McGuire, J. J. Mock, C. Ciracì, R. T. Hill, B. J. Wiley, A. Chilkoti and D. R. Smith, *Nano Lett.*, 2013, **13**, 5866-5872.
16. T. A. F. König, P. A. Ledin, J. Kerszulis, M. A. Mahmoud, M. A. El-Sayed, J. R. Reynolds and V. V. Tsukruk, *ACS Nano*, 2014, **8**, 6182-6192.
17. A. Moreau, C. Ciraci, J. J. Mock, R. T. Hill, Q. Wang, B. J. Wiley, A. Chilkoti and D. R. Smith, *Nature*, 2012, **492**, 86-89.
18. J. J. Mock, R. T. Hill, A. Degiron, S. Zauscher, A. Chilkoti and D. R. Smith, *Nano Letters*, 2008, **8**, 2245-2252.
19. J. Geldmeier, T. König, M. A. Mahmoud, M. A. El-Sayed and V. V. Tsukruk, *Adv. Func. Mater.*, 2014, n/a-n/a.
20. V. G. Kravets, F. Schedin, R. Jalil, L. Britnell, R. V. Gorbachev, D. Ansell, B. Thackray, K. S. Novoselov, A. K. Geim, A. V. Kabashin and A. N. Grigorenko, *Nat Mater*, 2013, **12**, 304-309.
21. L. Malassis, P. Massé, M. Tréguer-Delapierre, S. Mornet, P. Weisbecker, P. Barois, C. R. Simovski, V. G. Kravets and A. N. Grigorenko, *Adv. Mater.*, 2014, **26**, 324-330.
22. S. Thongrattanasiri, F. H. L. Koppens and F. J. García de Abajo, *Phys. Rev. Lett.*, 2012, **108**, 047401.
23. M. B. Müller, C. Kuttner, T. A. F. König, V. V. Tsukruk, S. Förster, M. Karg and A. Fery, *ACS Nano*, 2014, **8**, 9410-9421.
24. M. Svedendahl, P. Johansson and M. Käll, *Nano Lett.*, 2013, **13**, 3053-3058.
25. K. Aydin, V. E. Ferry, R. M. Briggs and H. A. Atwater, *Nat. Commun.*, 2011, **2**, 517.

26. B. Gao, G. Arya and A. R. Tao, *Nat. Nano.*, 2012, **7**, 433-437.
27. M. A. Mahmoud and M. A. El-Sayed, *J. Phys. Chem. C*, 2008, **112**, 14618-14625.
28. R. Kodiyath, S. T. Malak, Z. A. Combs, T. Koenig, M. A. Mahmoud, M. A. El-Sayed and V. V. Tsukruk, *J. Mater. Chem. A*, 2013, **1**, 2777-2788.
29. A. Tao, P. Sinsermsuksakul and P. Yang, *Nat. Nanotechnol.*, 2007, **2**, 435-440.
30. K. L. Genson, J. Holzmueller, C. Jiang, J. Xu, J. D. Gibson, E. R. Zubarev and V. V. Tsukruk, *Langmuir*, 2006, **22**, 7011-7015.
31. M. E. McConney, S. Singamaneni and V. V. Tsukruk, *Polym. Rev.*, 2010, **50**, 235-286.
32. H. J. Hagemann, W. Gudat and C. Kunz, *Journal of the Optical Society of America*, 1975, **65**, 742-744.
33. P. B. Johnson and R. W. Christy, *Phys. Rev. B*, 1972, **6**, 4370-4379.
34. V. P. Drachev, U. K. Chettiar, A. V. Kildishev, H.-K. Yuan, W. Cai and V. M. Shalaev, *Optics Express*, 2008, **16**, 1186-1195.
35. A. Klinkova, H. Thérien-Aubin, A. Ahmed, D. Nykypanchuk, R. M. Choueiri, B. Gagnon, A. Muntyanu, O. Gang, G. C. Walker and E. Kumacheva, *Nano Lett.*, 2014.
36. T. König, M. Weidemüller and A. Hemmerich, *Applied Physics B*, 2008, **93**, 545-549.
37. N. E. Christensen, *Phys. Status Solidi B*, 1972, **54**, 551-563.
38. A. Aubry, D. Y. Lei, S. A. Maier and J. B. Pendry, *Phys. Rev. Lett.*, 2010, **105**, 233901.
39. N. Grillet, D. Manchon, F. Bertorelle, C. Bonnet, M. Broyer, E. Cottancin, J. Lermé, M. Hillenkamp and M. Pellarin, *ACS Nano*, 2011, **5**, 9450-9462.
40. L. S. Slaughter, B. A. Willingham, W.-S. Chang, M. H. Chester, N. Ogden and S. Link, *Nano Lett.*, 2012, **12**, 3967-3972.
41. S. J. Barrow, D. Rossouw, A. M. Funston, G. A. Botton and P. Mulvaney, *Nano Lett.*, 2014, **14**, 3799-3808.
42. D. S. Citrin, *Nano Lett.*, 2005, **5**, 985-989.
43. B. Willingham and S. Link, *Optics Express*, 2011, **19**, 6450-6461.
44. H. Raether, *Surface plasmons on smooth and rough surfaces and on gratings*, Springer-Verlag, Berlin ; New York, 1988.
45. J. Homola, *Chem. Rev.*, 2008, **108**, 462-493.
46. M. Karg, T. A. F. König, M. Retsch, C. Stelling, P. M. Reichstein, T. Honold, M. Thelakkat and A. Fery, *Mater. Today*, 2014.